Bayesian Calibration of Resistance Spot Welding Models Using Temporal Process Features and Streamlined Active Learning

B. Verkens[1,2*], P. Li[3], L. Bogaerts[1,2], M. Faes[4,5], P. Van Rymenant[1] and D. Moens[1,2]

[1)] *KU Leuven, Department of Mechanical Engineering*
Jan Pieter de Nayerlaan 5, 2860 Sint-Katelijne-Waver, Belgium
email: {bouwe.verkens, patrick.vanrymenant, david.moens}@kuleuven.be
[2)] *FlandersMake@KU Leuven, Belgium*
[3] *Key Laboratory of Urban Security and Disaster Engineering of Ministry of Education, Beijing University of Technology, Beijing 100124, China*
email: li.peipei@bjut.edu.cn
[4)] *TU Dortmund, Chair for Reliability Engineering*
Leonhard-Euler-Strasse 5, 44227 Dortmund, Germany
email: matthias.faes@tu-dortmund.de
[5)] *Tongji University, International Joint Research Center for Engineering Reliability and Stochastic Mechanics, Shanghai 200092, China*

Abstract. Accurate multi-physics finite element modelling of resistance spot welding (RSW) remains challenging due to the uncertainties in contact and material parameters that shape the coupled thermal–electrical–mechanical process. This study introduces a Bayesian calibration framework, in contrast to the deterministic parameter optimisation approaches commonly adopted in existing RSW literature, which neglect the inherent variability of the welding process. The proposed framework performs calibration using multivariate model outputs, combining weld nugget geometry with geometrical and temporal attributes (El Ouafi et al., 2012) extracted from process signals such as dynamic resistance and electrode displacement. These features provide physically interpretable information on process evolution while reducing redundancy and correlation relative to full time-series data, enabling more effective parameter identifiability than nugget-only calibration. The methodology is applied to a 2D axisymmetric finite element model of RSW implemented in Simufact. In addition to the electrical and thermal contact parameters, a modified thermal conductivity formulation is introduced and treated as an unknown parameter to be inferred. Bayesian inference is performed using the Streamlined Bayesian Active Learning Cubature (SBALC) method (Li et al., 2025), with experimental multi-physics data (including nugget diameter and height, as well as process signals) used to infer posterior distributions for key modelling input variables.

Keywords: Resistance spot welding; Bayesian calibration; parameter inference

1. Introduction

Resistance spot welding (RSW) is a joining process process in which coupled thermal, electrical, and mechanical fields interact to form a fusion nugget between multiple metal sheets in milliseconds. To ensure structural reliability of the joints, there is an increasing demand for real-time quality monitoring of the welds. Modern monitoring algorithms rely on data-driven techniques that require large, diverse and well-labeled datasets (Xia et al., 2025). However, experimental data aquisition (process signal collection and quality metrics) is costly and time-consuming, resulting in machine-learning models that struggle to generalize to new materials, stack-ups, or production environments. At the same time, multi-physics finite element (FE) models of RSW have advanced considerably. Recent research approximate molten metal convection without explicitly modelling the flow field by introducing an enhanced thermal conductivity (Xia et al., 2023). A simultaneous simulation of nugget growth and process signals such as dynamic resistance and electrode displacement is achieved. Building on this, Lv et al. incorporate servo-gun dynamics and propose a rapid model generalization strategy across different steel grades and stack-up configurations through recalibration of contact parameters.

The accuracy of these FE models remains strongly dependent on uncertain model parameters, such as electrical and thermal contact properties between the plates and electrodes, whose true values may vary from weld to weld (Xia et al., 2023; Verkens et al., 2024). Traditional calibration techniques rely on tuning these unknown parameters by evaluating model output against measured nugget geometry and/or time-series data. Although this approach is widely applied, it inherently treats the modelling process as deterministic, which neglects the industrial variability and epistemic uncertainty present in RSW. Moreover, the resulting inverse problem is often ill-posed, admitting multiple parameter combinations that fit the data comparably well, and gradient-based solvers can become trapped in local minima. This motivates a calibration framework that is robust to modeling error, delivers uncertainty on inferred parameters and predictions, and remains computationally feasible for multi-physics FE models.

Bayesian calibration offers a framework for this problem (Kennedy and O'Hagan, 2001). Rather than producing a single point estimate, it yields a posterior probability distribution over the uncertain parameters, fully quantifying the remaining uncertainty given the available data. The main challenge to applying traditional Bayesian calibration techniques to high-fidelity RSW models is it's computational cost, since each forward model evaluation is expensive (Bogaerts et al., 2024). Recent research in these techniques has provided an elegant solution for this by modelling the likelihood function directly and reducing the amount of forward model evaluations substantially (Li et al., 2025).

A comprehensive calibration of the multi-physical RSW model necessitates the use of both weld quality measures, such as nugget diameter and thickness, as well as the characteristic process signals, such as dynamic resistance and electrode force, recorded during welding. These signals contain valuable information about the evolution of the weld across different physical fields (El Ouafi et al., 2012; American Welding Society et al., 2023), yet directly using full time-series data would lead to a very high-dimensional calibration problem. Moreover, as process measurements such as dynamic resistance and electrode force are long time series with high autocorrelation, treating the full time series as the calibration target introduces numerical difficulties in likelihood construction and Gaussian process (GP) surrogate modelling. To overcome these difficulties, this paper proposes compressing the time-series model outputs into a small set of physically motivated scalar features prior to calibration. This reduces the dimensionality of the calibration target, tackles the numerical issues associated with high autocorrelation in likelihood construction and GP surrogate modelling, while maintaining the physical information carried by these process signals.

The remainder of this paper is structured as follows. Section 2 describes the RSW finite element model, the uncertain parameters, and the extraction of scalar calibration features from the model outputs. A global sensitivity analysis identifies which parameters most strongly influence which features, and the selected features are used to define the calibration target. Section 3 reports the results of a preliminary parameter study, the sensitivity analysis, and a first application of SBALC to the RSW model. Section 4 discusses the findings and outlines directions for future work.

2. Methodology

2.1. Restistance spot welding model

The RSW process is modelled as a 2D axisymmetric coupled thermal–electrical–mechanical finite element model, implemented in Simufact Forming 2026.1. The forward model is denoted $\mathcal{M}(\mathbf{x}, \theta)$, where $\mathbf{x}$ are the known process parameters (welding current, welding time, electrode force) and $\theta \in \mathbb{R}^d$ are the uncertain model parameters to be inferred. In this work, $\mathbf{x}$ is fixed to a single welding schedule, so that $\mathcal{M}(\mathbf{x}, \theta)$ reduces to $\mathcal{M}(\theta)$ for the remainder of the paper.

The stack-up consists of two 1 mm thick DP1200 steel sheets. The electrode caps are truncated-cone copper electrodes with a cap diameter of 15.8 mm, a face diameter of 5.5 mm, and a tip radius of curvature of 30 mm, following the geometry used in (Verkens et al., 2024). The welding schedule applies an electrode force of 3 kN, followed by a welding current of 8 kA for 150 ms with a 10 ms ramp-up and 10 ms ramp-down. The simulation terminates 10 ms after the current reaches zero; the hold phase is not modelled.

The mesh uses quadtree elements with a base edge length of 0.25 mm. A level-2 refinement is applied within a bounding box around the weld zone, yielding a minimum element size of approximately 0.0625 mm in the contact region.

2.1.1. *Contact model*

The electrical contact resistance (ECR) at the electrode/sheet (E/S) and sheet/sheet (S/S) interfaces is modelled using the Bay-Wanheim formulation implemented in Simufact. The contact resistivity ρ is computed as:

$$\rho = 3 \cdot \frac{\sigma_{\text{soft}}}{\sigma_n} \cdot \frac{\rho_1 + \rho_2}{2} + \rho_c \,, \tag{1}$$

where σ_{soft} is the flow stress of the softer contact material, σ_n is the contact normal stress, ρ_1 and ρ_2 are the bulk resistivities of the two contact materials, and ρ_c is the coating resistivity. The electrical contact conductance is then obtained by dividing by the film thickness t_f. Two parameters per interface (E/S and S/S) are treated as uncertain: the film thickness t_f and the coating resistivity ρ_c.

The thermal contact resistance (TCR) is computed using a Simufact-specific formulation:

$$\mathrm{HTC} = P_1 \left(\frac{c_1 + c_2}{2}\right) \frac{1}{P_2} \left(1 - e^{-P_3\left(\frac{F_n}{\sigma_d} + P_3\right)}\right)^{P_4}, \tag{2}$$

where c_1 and c_2 are the thermal conductivities of the contact pair, F_n is the contact normal stress, σ_d is the yield stress, and P_1, P_2, P_3, P_4 are constants. The constants P_2, P_3, and P_4 are fixed at their Simufact default values; only P_1 is treated as an uncertain parameter. The value of P_1 directly influences the temperature difference across the interfaces and consequently affects the nugget shape and process signals (Lv et al., 2025).

2.1.2. *Modified thermal conductivity*

Standard FE formulations of RSW neglect fluid flow in the molten weld pool (Li et al., 2011), leading to unrealistically high predicted peak temperatures. Following Lv et al. (Lv et al., 2025), the thermal conductivity of the DP1200 steel is set to an elevated value λ_m above the melting temperature:

$$\lambda(T) = \begin{cases} \lambda_(T), & T < T_{\text{melting}}, \\ \lambda_m, & T \geq T_{\text{melting}}, \end{cases} \tag{3}$$

where $\lambda_(T)$ is the temperature-dependent thermal conductivity from the material database and $T_{\text{melting}} = 1507\,^\circ\mathrm{C}$ is the melting point of DP1200. The elevated value λ_m approximates the enhanced heat transport due to convective mixing in the weld pool.

2.1.3. *Uncertain parameters*

Six uncertain model parameters are considered for calibration, collected in the vector $\theta \in \mathbb{R}^6$. Due to the symmetric stack-up, the lower electrode/lower plate contact is assumed to share the same parameters as the upper electrode/upper plate contact. The prior distributions and bounds are summarised in Table I. For parameters spanning several orders of magnitude (t_f, ρ_c, and P_1), the prior is defined as uniform in $\log_{10}$-space, ensuring equal prior weight per order of magnitude. The modified thermal conductivity λ_m is assigned a uniform prior in physical space.

Table I. Unknown model parameters with prior distributions and bounds.

#	Symbol	Description	Unit	Prior bounds
1	$t_{f,\mathrm{S/S}}$	Film thickness, S/S interface	mm	$[1 \times 10^{-4},\ 5 \times 10^{-1}]^*$
2	$\rho_{c,\mathrm{S/S}}$	Coating resistivity, S/S interface	$\Omega \cdot \mathrm{m}$	$[5 \times 10^{-7},\ 5 \times 10^{-5}]^*$
3	$t_{f,\mathrm{E/S}}$	Film thickness, E/S interface	mm	$[1 \times 10^{-4},\ 5 \times 10^{-1}]^*$
4	$\rho_{c,\mathrm{E/S}}$	Coating resistivity, E/S interface	$\Omega \cdot \mathrm{m}$	$[5 \times 10^{-7},\ 5 \times 10^{-5}]^*$
5	P_1	HTC scaling constant	–	$[1 \times 10^{-3},\ 1 \times 10^{-1}]^*$
6	λ_m	Thermal conductivity above melting	W/(m·K)	$[35,\ 200]$

* Prior is uniform in $\log_{10}$-space.

Parameters 1–4 govern the electrical contact interactions at the two interface types through Equation 1. Parameter P_1 scales the heat transfer from the sheets to the electrodes via Equation 2, and λ_m governs the heat redistribution within the molten nugget. Uninformative uniform priors are assigned to all parameters:

$$\theta_i \sim \mathcal{U}(\theta_i^{\min}, \theta_i^{\max}), \quad i = 1, \ldots, 6. \tag{4}$$

2.2. Calibration targets: feature extraction from model outputs

The forward model $\mathcal{M}(\theta)$ produces both scalar outputs (nugget geometry) and time-series signals (dynamic resistance, temperature history, electrode displacement). Using full time-series data as calibration targets is problematic for surrogate-based Bayesian methods. Process signals such as dynamic resistance are generated by a system of coupled partial differential equations driven by a time-varying current input. Therefore successive samples carry almost identical information about θ. Treating m such samples as independent under a diagonal covariance $\Sigma = \mathrm{diag}(\sigma_1^2, \ldots, \sigma_m^2)$ amounts to counting the same physical discrepancy m times, resulting in a sharper log-likelihood surface, which produces an overconfident posterior. A peaked log-likelihood surface causes two numerical failures in the SBALC framework: the GP surrogate requires an extremely short kernel length scale to fit the narrow likelihood and the active learning loop clusters new evaluation points in a shrinking neighbourhood of the optimum causing the GP covariance matrix to be ill-conditioned and Cholesky factorisation can fail.

The solution adopted in this work is to extract a small set of physically motivated scalar features from the time-series outputs prior to calibration. This reduces the residual dimension from m to $p \ll m$, broadens the likelihood surface by eliminating the pseudo-replication effect, and avoids the numerical fragility described above. As the resulting features are scalar quantities with distinct physical origins, a diagonal covariance $\Sigma \in \mathbb{R}^{p \times p}$ is an appropriate noise model. In this work the following features extracted from the RSW FE model are used:

Nugget geometry. The FE model produces a set of geometric metrics describing the weld nugget and contact zone, including nugget height and width (at both liquidus and solidus isotherms), joint penetration depth into each sheet, electrode/sheet contact width, indentation depth, and minimum remaining solid sheet thickness.

Dynamic resistance features The dynamic resistance (DR) curve is a time-varying signal that reflects the evolution of electrical resistance during the welding stage. Rather than using the full DR signal, scalar features are extracted following the geometrical characterisation approach of El Ouafi et al. (El Ouafi et al., 2012). Candidate features include: the resistance values at the first inflection point (R_α), the peak (R_β), and the final value (R_γ); the corresponding times (t_α, t_β, t_γ); the slopes before and after the peak (m_1, m_2); the mean resistance (R_m); and the resistance drops $dR_1 = R_\beta - R_\alpha$ and $dR_2 = R_\gamma - R_\beta$.

The peak resistance R_β is primarily driven by the bilinear relationship between sheet resistivity and temperature, while the post-peak resistance drop is dominated by the increase of the electrode/sheet contact diameter (American Welding Society et al., 2023).

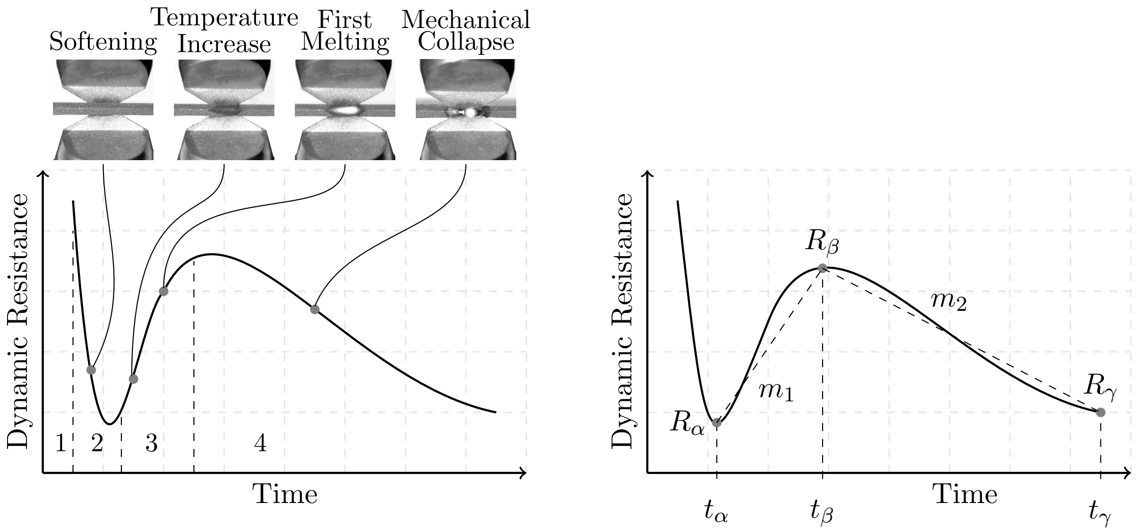

Figure 1. Schematic representation of dynamic resistance features. (Left) Theoretical dynamic resistance curve with weld nugget evolution stages, adapted from Dickinson et al. (Dickinson et al., 2013). The upper images illustrate the nugget evolution captured by a Phantom VEO 640 high-speed camera (Bogaerts et al., 2023). (Right) Selected geometrical features extracted from the dynamic resistance curve, adapted from El Ouafi et al. (El Ouafi et al., 2012).

Maximum sheet temperature The peak temperature in the upper and lower sheets during welding. This quantity is directly sensitive to λ_m (higher λ_m reduces the peak temperature) and P_1 (which controls the heat transfer at the interfaces).

Electrode displacement features. The electrode displacement signal records the relative motion of the upper electrode during welding. While welding, the the upper electrode moves due to thermal expansion of the heated sheets and nugget growth. Four scalar features are extracted from the displacement signal $S(t)$, with a 2 ms margin trimmed from the start of the welding stage to exclude the initial settling transient. Let S_0 denote the displacement at the start of the trimmed interval and S_{peak} the maximum displacement reached. The peak expansion $\Delta S_P = S_{\mathrm{peak}} - S_0$ captures the total thermal expansion during nugget growth. The end-of-welding displacement S_{end} and the net displacement $\Delta S_{\mathrm{net}} = S_{\mathrm{end}} - S_0$ reflect the residual deformation after current shut-off and partial cooling. The expansion rate $\dot{S}_{\mathrm{exp}}$ is obtained as the slope of a linear fit to $S(t)$ from the start of welding to the time of peak displacement, providing a measure of the nugget growth rate.

For $d = 6$ unknown parameters, at least $p \geq 6$ features with approximately linearly independent sensitivities are required to ensure identifiability. The sensitivity analysis in Section 2.3 is used to select the most informative subset.

2.3. Global sensitivity analysis

To quantify the influence of each uncertain parameter on the model outputs and to guide feature selection for calibration, a variance-based global sensitivity analysis is performed using Sobol indices

(Sobol, 2001). A Design of Experiments (DoE) of 90 samples is generated from the six-dimensional prior distribution using a Latin Hypercube design. Each sample requires a full forward model evaluation in Simufact. One simulation failed to converge, leaving 88 successful runs. From each simulation, 18 scalar output features are extracted, grouped into four categories:

- *Dynamic resistance* (3 features): peak resistance R_β, end-of-welding resistance R_γ, and mean resistance R_m. These are extracted from a Savitzky–Golay-smoothed DR signal (3rd-order polynomial, window size 11), with a 2 ms margin trimmed from both ends of the welding stage to avoid transient artefacts.
- *Electrode displacement* (4 features): peak expansion $\Delta S_P = S_{\text{peak}} - S_0$, end-of-welding displacement S_{end}, net displacement $\Delta S_{\text{net}} = S_{\text{end}} - S_0$, and expansion rate $\dot{S}_{\text{exp}}$ (slope of a linear fit to the displacement signal from the start of welding to the peak).
- *Sheet temperature* (4 features): maximum temperature across both sheets $T_{\max}$, time to reach peak temperature $t(T_{\max})$, end-of-simulation temperature T_{end}, and cooling rate $\dot{T}_{\text{cool}}$ (computed as the slope from $T_{\max}$ to T_{end}).
- *Nugget geometry* (7 features): nugget width and height at the liquidus isotherm ($d_{\text{n,liq}}$, $h_{\text{n,liq}}$) and solidus isotherm ($d_{\text{n,sol}}$, $h_{\text{n,sol}}$), electrode/sheet contact width w_{elec}, indentation depth d_{indent}, and minimum remaining unmolten sheet thickness t_{unmolt}.

A Polynomial Chaos Expansion (PCE) surrogate is fitted to the 88 successful runs using the Least Angle Regression Sparse (LARS) algorithm (Blatman and Sudret, 2011) with candidate polynomial degrees 1 through 5, as implemented in UQLab (Marelli and Sudret, 2014). The leave-one-out (LOO) cross-validation error is used to assess the quality of the surrogate for each output. First-order and total-order Sobol indices are then computed analytically from the PCE coefficients at no additional computational cost. The first-order Sobol index of parameter θ_i on output Y is:

$$S_i = \frac{\mathrm{Var}[\mathbb{E}(Y \mid \theta_i)]}{\mathrm{Var}(Y)}, \tag{5}$$

and the total-order index, which includes all interaction effects, is:

$$S_{T_i} = 1 - \frac{\mathrm{Var}[\mathbb{E}(Y \mid \boldsymbol{\theta}_{\sim i})]}{\mathrm{Var}(Y)}, \tag{6}$$

where $\boldsymbol{\theta}_{\sim i}$ denotes all parameters except θ_i. Second-order interaction indices are also computed to identify parameter pairs with coupled effects on specific outputs. The results of this analysis are presented and discussed in Section 3.2.

2.4. Bayesian model calibration

The calibration framework follows the Bayesian approach described in (Kennedy and O'Hagan, 2001). Given observations Y_{obs}, Bayes' theorem updates the prior distribution $f(\theta)$ to the posterior:

$$f(\theta \mid Y_{\text{obs}}) = \frac{L(Y_{\text{obs}} \mid \theta)\, f(\theta)}{c}, \tag{7}$$

where $L(Y_{\text{obs}} \mid \theta)$ is the likelihood function and $c = \int L(Y_{\text{obs}} \mid \theta)\, f(\theta)\, \mathrm{d}\theta$ is the model evidence. Assuming Gaussian measurement error with zero mean and covariance Σ, the log-liklihood for N_{obs} independent observation replicates is:

$$\ln L(\theta) = \mathscr{L}(\theta) = -\frac{1}{2} \sum_{k=1}^{N_{\text{obs}}} r_k(\theta)^{\top} \Sigma^{-1} r_k(\theta) + \text{const}, \tag{8}$$

where $r_k(\theta) = Y_{\text{obs}}^{(k)} - \mathcal{M}(\theta)$ is the residual between the k-th observation and the model response. As the calibration targets are scalar features with distinct physical origins rather than successive datapoints from an autocorrelated signal, a diagonal covariance Σ is appropriate and no full covariance estimation is required.

2.5. Streamlined Bayesian Active Learning Cubature (SBALC)

The posterior distribution in Equation 7 is evaluated using the SBALC method (Li et al., 2025), which fits a Gaussian Process (GP) surrogate directly to the log-likelihood function $\mathscr{L}(\theta)$ and uses active learning to minimise the number of forward model evaluations. The model evidence is estimated as:

$$\hat{c} = \mathbb{E}_{\theta}[\exp(\hat{m}_{\mathscr{L}_n}(\theta))]\,, \tag{9}$$

where $\hat{m}_{\mathscr{L}_n}$ is the GP posterior mean after n evaluations, with the expectation approximated by Monte Carlo over $N_M = 2 \times 10^4$ prior samples. At each iteration, the next evaluation point is selected by maximising the learning function:

$$\mathrm{LF}(\theta) = \sigma^2_{\mathscr{L}_n}(\theta) \cdot \left(e^{m_{\mathscr{L}_n}(\theta) + b\,\sigma_{\mathscr{L}_n}(\theta)} - e^{m_{\mathscr{L}_n}(\theta) - b\,\sigma_{\mathscr{L}_n}(\theta)} \right), \tag{10}$$

with $b = 1$. Iterations stop when the convergence ratio $|c_{\text{upper}} - c_{\text{lower}}|/\hat{c} < 0.1$ holds over two consecutive iterations. Posterior samples are generated via Sampling-Importance-Resampling (SIR) (Rubin and Rubin, 1988). A detailed derivation of the method is provided by Li et al..

3. Results

3.1. Preliminary parameter study

To confirm the expected physical influence of the parameters P_1 and λ_m and to verify consistency with the findings reported by Lv et al. (Lv et al., 2025), a preliminary one-at-a-time parameter study was performed. Five simulations were run with varying values of $P_1 \in [0.0005,\ 0.0025]$ (at fixed $\lambda_m = 35$ W/(m·K)) and eight with varying values of $\lambda_m \in [0,\ 200]$ W/(m·K) (at fixed $P_1 = 0.0005$). All contact parameters were held at their nominal values: $t_{f,\text{S/S}} = t_{f,\text{E/S}} = 10^{-5}$ mm and $\rho_{c,\text{S/S}} = \rho_{c,\text{E/S}} = 2.1 \times 10^{-6}$ Ω·m.

3.1.1. *Effect of thermal conductivity at melting λ_m.*

Figure 2 summarises the influence of λ_m on the peak resistance, the maximum sheet temperature, and the nugget geometry at the solidus isotherm. The peak resistance R_β is virtually unaffected by λ_m, which is expected since the DR signal is governed by the bulk and contact resistivities rather than by the thermal field inside the nugget. In contrast, the maximum sheet temperature decreases substantially with increasing λ_m. The elevated thermal conductivity redistributes heat within the molten pool, suppressing unrealistic temperature peaks. The nugget geometry responds accordingly: both the solidus diameter d_n and height h_n increase with λ_m as the thermal energy is spread more uniformly. The effect saturates for $\lambda_m \gtrsim 100$ W/(m·K), consistent with the findings of Lv et al. (Lv et al., 2025).

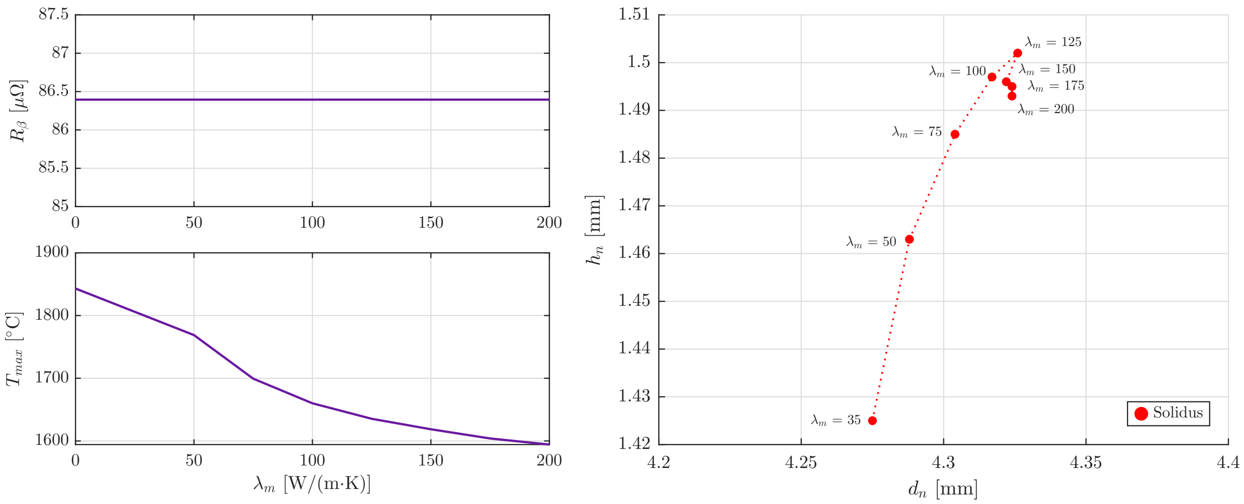

Figure 2. Influence of λ_m on peak resistance R_β (top left), maximum sheet temperature $T_{\max}$ (bottom left), and nugget geometry at the solidus isotherm (right).

3.1.2. *Effect of heat transfer coefficient scaling constant P_1.*

Figure 3 shows the influence of P_1 on the peak resistance, the peak displacemnt of the upper electrode, and the nugget geometry at both the liquidus and solidus isotherms. Increasing P_1 enhances the thermal contact conductance at the E/S interface, allowing more heat to flow from the sheets into the electrodes. This produces a moderate decrease in the peak resistance R_β and a reduction in the peak electrode expansion ΔS_P, both consistent with a cooler sheet surface. The effect on the nugget geometry is pronounced: as P_1 increases from 0.0005 to 0.0025, the nugget diameter d_n decreases while the nugget height h_n is reduced substantially (from approximately 2.1 mm to 1.5 mm at the liquidus isotherm). Physically, a higher HTC draws heat away from the weld zone through the electrodes, resulting in a smaller and flatter nugget.

These results confirm the findings of Lv et al. (Lv et al., 2025) and demonstrate that P_1 and λ_m have distinct and significant effects on the model outputs, motivating their inclusion as uncertain parameters in the Bayesian calibration. Notably, λ_m primarily affects the thermal field and nugget geometry while leaving the DR signal unchanged, whereas P_1 influences both the process signals and the nugget shape. This complementary sensitivity structure suggests that including both DR features and nugget geometry in the calibration target will aid in distinguishing the two parameters.

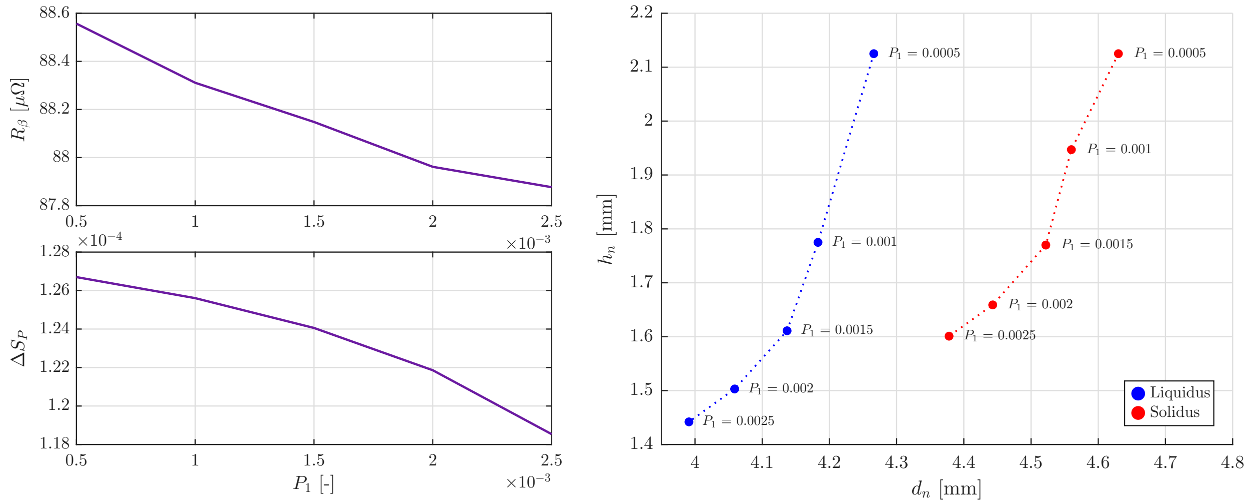

Figure 3. Influence of P_1 on peak resistance R_β (top left), peak electrode expansion ΔS_P (bottom left), and nugget geometry at the liquidus and solidus isotherms (right).

3.2. Global sensitivity analysis

Figure 4 and 5 present the first-order and total-order Sobol indices for all 18 output features with respect to the six uncertain parameters.

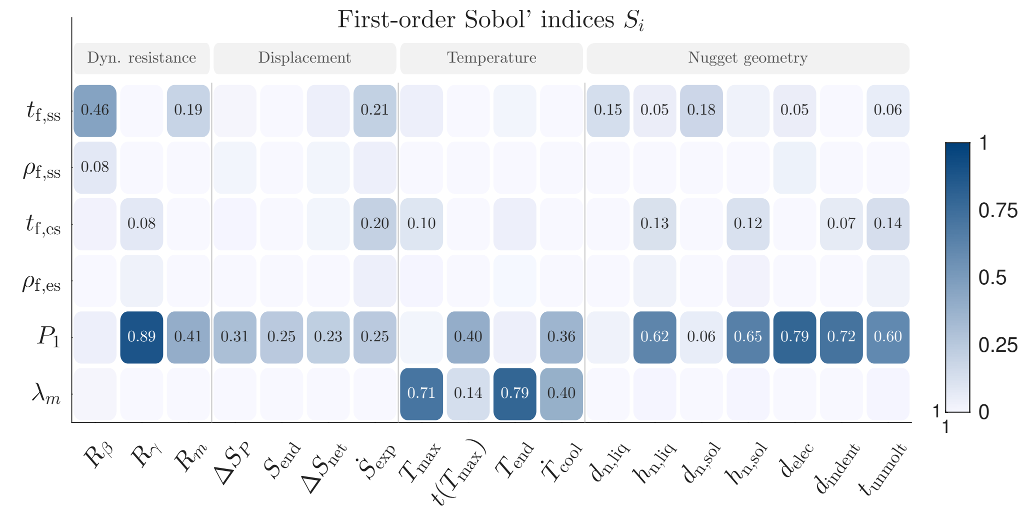

Figure 4. First-order Sobol indices for each output feature and uncertain parameter. Values below 0.05 are omitted for clarity.

The results show how each input parameter contributes to the variance of the features in the four output categories. Each parameter influences a distinct subset of output features, suggesting that the features provide complementary information for identifying the input parameters. The

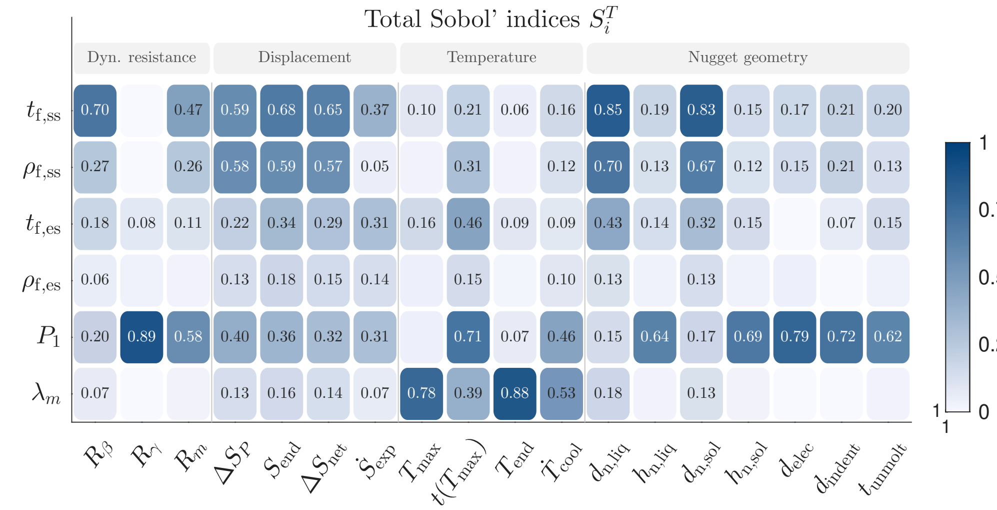

Figure 5. Total-order Sobol indices S_i^T for each output feature and uncertain parameter. Values below 0.05 are omitted for clarity.

parameter P_1 is the single most influential parameter overall. In the dynamic resistance features it dominates R_γ with a first order index of $S_i = 0.89$ and has a moderate influence on R_m. Its influence is spanning accros the other four output categories and is affecting the displacement features ($S_i = 0.25 - 0.31$), the temperature features ($S_i = 0.36 - 0.79$), and the nugget geometry, where the first-order indices range from 0.6 to 0.79. This is consistent with the physical role of P_1 as the HTC scaling constant, which controls the heat extraction through the electrodes.

The modified thermal conductivity λ_m has a complementary sensitivity pattern, with its influence concentrated on the temperature features ($S_1 = 0.71$ for $T_{\max}$ and 0.79 for $t(T_{\mathrm{end}})$). This confirms the observation from the preliminary parameter study (Section 3.1), as λ_m redistributes heat within the molten pool without affecting the electrical and mechanical response. The total-order indices for λ_m are larger than the first-order values, reaching $S_i^T = 0.78$ for $T_{\max}$ and 0.88 for $t(T_{\mathrm{end}})$, indicating interaction effects with other parameters on the temperature outputs.

The S/S film thickness $t_{f,\mathrm{S/S}}$ is the most influential contact parameter, with $S_1 = 0.46$ for the peak resistance R_β and smaller direct contributions to the liquidus nugget diameter $d_{n,\mathrm{liq}}$ ($S_i = 0.15$), the solidus nugget diameter $d_{n,\mathrm{sol}}$ ($S_i = 0.18$), and the expansion rate $\dot{S}_{\mathrm{exp}}$ ($S_i = 0.21$). However, its total-order indices are substantially larger across nearly all outputs, indicating that $t_{f,\mathrm{S/S}}$ acts heavily through interaction effects. The remaining S/S parameter $\rho_{c,\mathrm{S/S}}$ shows weak sensitivity overall, with only minor total-order contribution to the displacement peak resistance. Nevertheless, its total-order indices reveal substantial interaction contributions as well.

The E/S film thickness $t_{f,\mathrm{E/S}}$ has only small direct effects, with its largest contributions on $\dot{S}_{\mathrm{exp}}$, $T_{\max}$, and hn, liq. Its higher total-order indices indicate that its influence is mainly through interactions with other parameters. In contrast, the E/S coating resistivity $\rho_{f,\mathrm{E/S}}$ shows negligible sensitivity across all outputs ($S_i^T < 0.18$), suggesting that it has little effect and is difficult to identify from the data.

Feature selection for calibration. Based on the sensitivity analysis, ten features are selected for the calibration target vector $Y \in \mathbb{R}^{10}$: the peak resistance R_β, the peak electrode expansion ΔS_P, the maximum and end-of-simulation sheet temperatures $T_{\max}$ and T_{end}, the nugget width and height at both liquidus and solidus isotherms ($d_{\text{n,liq}}$, $h_{\text{n,liq}}$, $d_{\text{n,sol}}$, $h_{\text{n,sol}}$), the electrode contact width w_{elec}, and the indentation depth d_{indent}. Time-dependent features (t_α, t_β, $t(T_{\max})$) are excluded as the discrete time stepping of the FE solver introduces artificial quantisation that would degrade the smoothness of the likelihood surface. The selected features span all four output categories and collectively provide sensitivity to five parameters, with R_β and ΔS_P primarily targeting P_1 and the contact parameters, $T_{\max}$ and T_{end} targeting λ_m, and the nugget geometry features providing information on all parameters simultaneously.

3.3. Bayesian calibration

As a first step towards a full Bayesian calibration of all six unknown parameters, a single-parameter calibration is performed. Based on the Sobol analysis in Section 3.2, P_1 is selected as calibration parameter. The SBALC algorithm is applied with $P_1 \sim \mathcal{U}(0.0001, 0.1)$ as only unknown parameter, where R_γ is used as calibration feature. The initial design consists of $n_0 = 5$ Hammersley points and the convergence threshold is chosen as $b_{\text{cr}} = 0.1$.

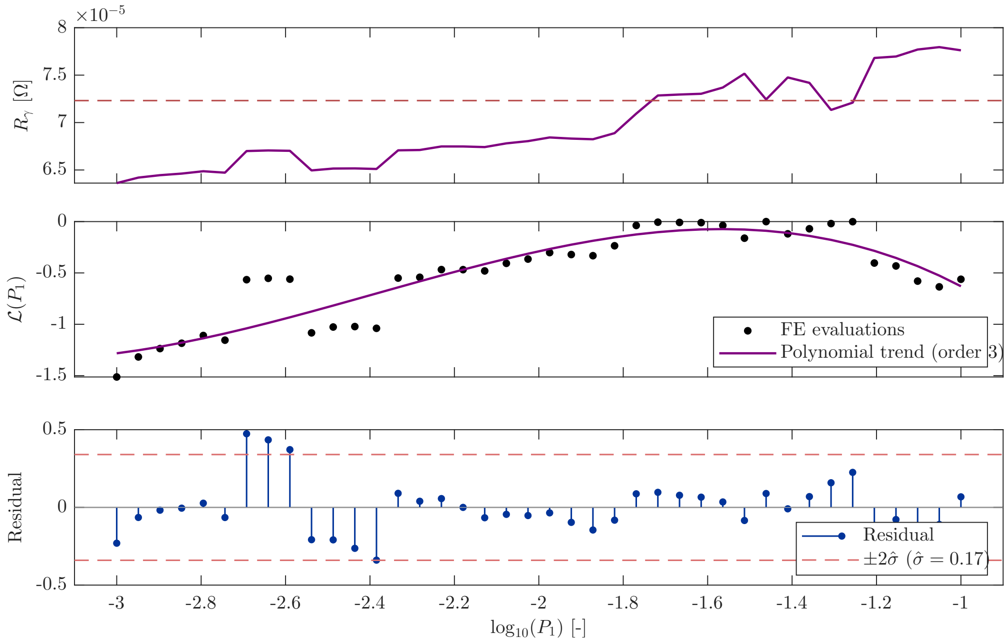

Figure 6. Diagnostic sweep over $\log_{10}(P_1)$. Top: model response R_γ with Y_{obs} (dashed). Middle: log-likelihood $\mathscr{L}(P_1)$ evaluated at each model response point. Bottom: residuals after detrending.

However, when SBALC is directly applied to the RSW FE model, no satisfactory convergence is reached. To investigate the cause of this behaviour, the log-likelihood is evaluated at 40 points over the prior range of P_1. The results are shown in Figure 6. In here we see that the log-likelihood follows a global trend, similar to the one observed in Section 3.1. On top of this trend, small deviations can be observed. These deviations correspond to deterministic numerical noise, which originates from mesh discretisation and adaptive time stepping in the FE model. Repeated evaluation at the same parameter values yields identical results, which indicates that the noise is not stochastic and cannot be reduced by averaging. It is an inherent artefact of the numerical discretisation.

This behaviour is problematic for SBALC, as the method uses a GP surrogate of the log-likelihood and assumes sufficient smoothness for accurate interpolation between a limited number of training points. If no noise model is included in the GP, the GP interpolates exactly through all training points, including the noise. As a result, the GP is overfitting, which influences both the learning function used to select new evaluation points and the convergence criterion based on the upper and lower bounds of the model evidence estimate. Li et al. acknowledge this limitation, noting that SBALC is restricted to likelihood-functions of moderate smoothness.

Resolving this issue requires modifying the GP fitting procedure to account for the deterministic noise, for instance by introducing a fixed nugget term in the GP covariance and separating the resulting epistemic and aleatoric contributions to the predictive variance. This extension is the subject of ongoing work and will be reported in a future publication.

4. Discussion and conclusions

This paper presents a Bayesian calibration framework for a 2D axisymmetric resistance spot welding finite element model with six uncertain parameters. This contrasts the current deterministic optimization approaches commonly used in RSW calibration. A key element of the approach presented here is the use of physical motivated features extracted from process signals, rather than using the full-time series. While full time-series would carry more information, the high autocorrelation of these signals (such as dynamic resistance and electrode displacement) leads to an narrow log-likelihood and numerical instabilities in the GP surrogate.

A preliminary parameter study confirmed that P_1 and λ_m have distinct and complementary effects on the model outputs. The parameter P_1 primarily governs the nugget geometry and process signals through its control of heat extraction at the electrode/sheet interface, whereas λ_m affects the temperature field and nugget dimensions without changing the dynamic resistance signal.

A global sensitivity analysis over all six model parameters revealed that P_1 influences most output features, while λ_m mostly influences the temperature response. The S/S interface is more influential than the E/S interface, with the film thickness $t_{f,\mathrm{S/S}}$ emerging as the most influential contact parameter contributing to both the resistance and nugget diameter. The E/S film thickness $t_{f,\mathrm{E/S}}$ showed negligible first-order sensitivity but substantial total-order indices on selected features, indicating that it acts through parameter interactions. Based on these results, ten calibration features are selected to use in further work.

A first application of SBALC to a single parameter calibration (P_1) revealed that deterministic numerical noise from mesh discretisation and adaptive time stepping in the FE model prevents convergence of the method. This noise is reproducible and cannot be reduced by repeated forward model evaluations, which distinguishes it from stochastic measurement noise. Addressing this limitation requires modifying the GP fitting to account for the deterministic noise, for instance by introducing a nugget term in the GP covariance. This extension, along with the full six-parameter calibration, is the subject of ongoing work.

Acknowledgements

The authors gratefully acknowledge the support of the Research Foundation – Flanders (FWO) under grant 1SE1423N, the internal funding of KU Leuven grant C24E/21/026 and the support of the Flemish Government through the Flanders Make.

References

American Welding Society, Y.-J. Xia, T.-L. Lv, Y.-B. Li, H. Ghassemi-Armaki, and B. E. Carlson: 2023, 'Quantitative Interpretation of Dynamic Resistance Signal in Resistance Spot Welding'. *Welding Journal* **102**(4), 69–87.

Blatman, G. and B. Sudret: 2011, 'Adaptive sparse polynomial chaos expansion based on *least angle regression*'. *Journal of Computational Physics* **230**(6), 2345–2367.

Bogaerts, L., A. Dejans, M. G. R. Faes, and D. Moens: 2023, 'A machine learning approach for efficient and robust resistance spot welding monitoring'. *Welding in the World*.

Bogaerts, L., M. G. Faes, and D. Moens: 2024, 'A Data Driven Black Box Approach for the Inverse Quantification of Set-Theoretical Uncertainty'. *ASCE-ASME J Risk and Uncert in Engrg Sys Part B Mech Engrg* **11**(031201).

Dickinson, D. W., J. E. Franklin, and A. Stanya: 2013, 'Characterization of Spot Welding Behavior by Dynamic Electrical Parameter'.

El Ouafi, A., R. Belanger, and M. Guillot: 2012, 'Dynamic Resistance Based Model for On-Line Resistance Spot Welding Quality Assessment'. *Materials Science Forum* **706-709**, 2925–2930.

Kennedy, M. C. and A. O'Hagan: 2001, 'Bayesian Calibration of Computer Models'. *Journal of the Royal Statistical Society Series B: Statistical Methodology* **63**(3), 425–464.

Li, P.-P., C. Dang, C. H. Acevedo, M. A. Valdebenito, and M. G. R. Faes: 2025, 'Bayesian model updating via streamlined Bayesian active learning cubature'. arXiv:2509.11204 [stat].

Li, Y. B., Z. Q. Lin, Q. Shen, and X. M. Lai: 2011, 'Numerical analysis of transport phenomena in resistance spot welding process'. *Journal of Manufacturing Science and Engineering, Transactions of the ASME* **133**(3), 1–8. Number: 3.

Lv, T.-L., Y.-J. Xia, S. P. Murugan, F. Okigami, H. Ghassemi-Armaki, B. E. Carlson, and Y. Li: 2025, 'Multi-physical process simulation of resistance spot welding available for synthetic data generation'. *Journal of Manufacturing Processes* **141**, 709–724.

Marelli, S. and B. Sudret: 2014, 'UQLab: A Framework for Uncertainty Quantification in Matlab'. pp. 2554–2563. Publisher: American Society of Civil Engineers.

Rubin, D. and D. Rubin: 1988, 'Using the SIR algorithm to simulate posterior distributions'.

Sobol, I.: 2001, 'Global sensitivity indices for nonlinear mathematical models and their Monte Carlo estimates'. *Mathematics and Computers in Simulation* **55**(1-3), 271–280.

Verkens, B., M. Faes, P. Van Rymenant, and D. Moens: 2024, 'Towards industrial relevance: Uncertainty in numerical resistance spot welding models'. In: *9th European Congress on Computational Methods in Applied Sciences and Engineering*. CIMNE.

Xia, Y.-J., T.-L. Lv, H. Ghassemi-Armaki, Y.-B. Li, and B. E. Carlson: 2023, 'Collaborative Simulation of Nugget Growth and Process Signals for Resistance Spot Welding'. *Welding in the World* **67**(6), 1377–1392. Company: Springer Distributor: Springer Institution: Springer Label: Springer Number: 6 Publisher: Springer Berlin Heidelberg.

Xia, Y.-J., Q. Song, B. Yi, T. Lyu, Z. Sun, and Y. Li: 2025, 'Improving out-of-distribution generalization for online weld expulsion inspection using physics-informed neural networks'. *Welding in the World* **69**(5), 1309–1322.